International Journal of Microwave and Wireless Technologies

cambridge.org/mrf

Wideband glass resonator antenna array for D-band applications

Mario Faliero, Thomas Zwick and Akanksha Bhutani

Institute of Radio Frequency Engineering and Electronics (IHE), Karlsruhe Institute of Technology (KIT), Germany

Research Paper

Cite this article: Faliero M, Zwick T, Bhutani A (2026) Wideband glass resonator antenna array for D-band applications. *International Journal of Microwave and Wireless Technologies*, 1–11. https://doi.org/10.1017/S1759078726103948

Received: 3 January 2026 UTC
Revised: 21 September 2026 UTC
Accepted: 27 September 2026 UTC

Keywords:
antenna-in-package (AiP); dielectric resonator antenna; glass; laser ablation; micromachining; millimeter wave antennas; permittivity; vapor deposition

Corresponding author: Mario Faliero; Email: mario.faliero@outlook.com

Abstract

This paper presents the design of a wideband pyramidal inverted glass resonator antenna (PIGRA) for sub-terahertz applications. The proposed glass antenna concept is demonstrated through two implementations: (i) a single radiator integrated on a single-layer glass Printed Circuit Board (PCB) based on a glass-on-glass architecture, and (ii) a 4×4 planar square PIGRA array implemented on a two-layer Rogers CLTE substrate. The single-radiator implementation achieves an impedance bandwidth exceeding 42 %, covering the entire D-band (110–170 GHz), with a peak realized gain of 5.8 dBi. The 4×4 array achieves a 38 % impedance bandwidth in D-band, and a peak realized gain of 15 dBi. The proposed antenna is fabricated using laser-induced deep etching (LIDE®) technology from LPKF® on Schott® BF33 borosilicate glass, demonstrating for the first time the feasibility of 2.5D glass micromachining for antenna structures operating at frequencies above 100 GHz. The glass PCB of the single-radiator implementation is metallized through physical vapor deposition, followed by an electroplating process. The design methodology, fabrication process, assembly approach, and measured performance are presented and compared with full-wave electromagnetic simulation results obtained using CST Microwave Studio. The measured results are in good agreement with the simulations and validate the proposed glass-based PIGRA architecture for D-band and beyond wireless communication and sensing applications.

Introduction

An earlier version of this work was presented at the 55th European Microwave Conference (EuMW, 2025) and published in its Proceedings [1]. That paper introduced the preliminary analysis and design and electromagnetic analysis of a borosilicate glass pyramidal inverted dielectric resonator antenna (PIGRA) for sub-terahertz (sub-THz) applications (Figure 1). The present paper significantly extends the preliminary work by presenting the complete design, fabrication, and experimental validation of a 4×4 PIGRA array operating across the entire D-band (Figure 2).

The limited availability of radio frequency (RF) spectrum and the increasing demand for higher data rates have driven research toward frequencies beyond 100 GHz. The 110–170 GHz frequency range (D-band) is considered a promising candidate for future wireless communications (6G and beyond), as well as for autonomous driving, radar, and sensing applications, due to its large available bandwidth and high level of technology readiness [2]. At millimeter-wave (mmWave) frequencies, enabling capabilities such as high data rates, massive MIMO (Multi Input Multi Output), high resolution, and high integration density become feasible [3].

Semiconductor technologies have demonstrated transistors with maximum oscillation frequencies exceeding 600 GHz [4]. However, as the operating frequency increases, conductor ohmic losses rise significantly, fabrication tolerances become more stringent, and system integration becomes more challenging. Consequently, the losses associated with transceiver–antenna interconnect increase, while the radiation efficiency of metallic antennas degrades rapidly.

As discussed in [1], the antenna-in-package (AiP) concept aims to mitigate interconnection losses by reducing the distance between the transceiver chip and the antenna (Figure 3), while facilitating system integration and mass-production manufacturability [5–7].

Dielectric resonator antennas (DRAs) do not suffer from ohmic losses and offer compact size, low thermal expansion, and high radiation efficiency due to the absence of metallic radiating elements, although they typically provide low-to-moderate gain [8]. Employing DRAs in array configurations increases the effective isotropic radiated power by enhancing antenna gain, thereby compensating for the significant path loss encountered at mmWave frequencies [9]. Dielectric resonators [10] made of low-loss ($\tan\delta \approx 10^{-3}$) and high-permittivity ($\epsilon_r > 30$ [11])

© The Author(s), 2026. Published by Cambridge University Press in association with The European Microwave Association. This is an Open Access article, distributed under the terms of the Creative Commons Attribution licence (http://creativecommons.org/licenses/by/4.0), which permits unrestricted re-use, distribution and reproduction, provided the original article is properly cited.

Downloaded from https://www.cambridge.org/core. Karlsruher Institut fuer Technologie (KIT), on 19 Nov 2026 at 11:26:45, subject to the Cambridge Core terms of use, available at https://www.cambridge.org/core/terms. https://doi.org/10.1017/S1759078726103948

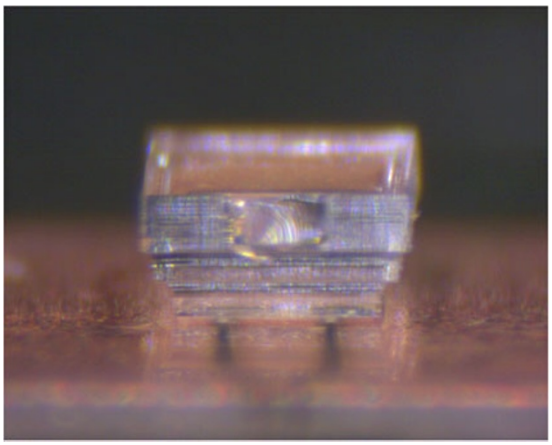
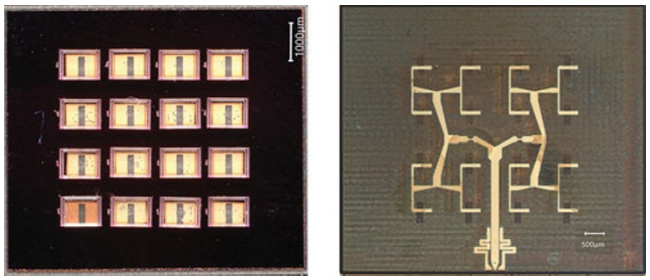


Figure 1. Pyramidal inverted glass resonator on glass PCB.



(a): PIGRAs arrangement. (b): 1:16 feed network.

Figure 2. Pyramidal inverted glass resonator on glass PCB.

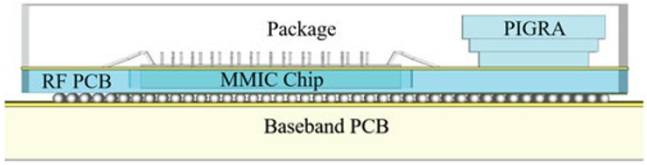


Figure 3. PIGRA MMIC package concept.

dielectric material have been used in microwave circuitry for decades as high-Q filter components [12]. Conversely, DRAs require a relatively low Q-factor to achieve wider impedance bandwidths [13–15]. Typical DRAs provide impedance bandwidths of approximately 30%, which are insufficient to cover the entire D-band, while the realized gain of single resonator operating in its fundamental mode is generally below 6 dBi, with a small resonator operating around the lowest mode [8, 24]. Different techniques have been reported to enhance the operating bandwidth [16], including stacking multiple resonators [17–19], reducing the dielectric permittivity, employing different resonator geometries [16, 20], introducing parasitic radiators [21], using frequency selective surface superstrates [22], and incorporating surface-mounted horn [23].

In this paper, a wideband glass-based pyramidal inverted resonator antenna is proposed as the radiating element of a D-band planar antenna array, as shown in Figure 2. The proposed radiating element is intended for integration into a monolithic microwave integrated circuit (MMIC) package for mmWave applications (Figure 3). The PIGRA exhibits an intrinsic impedance bandwidth exceeding 40% (for $|S_{11}| \leq -10$ dB) covering the entire D-band. The wide bandwidth is achieved mainly by the tapered vertical cross-section, which enables the excitation of multiple resonant modes over the operating frequency range.

For this design, Schott Borofloat 33 (BF33) borosilicate glass was selected as the material for manufacturing the PIGRA due to its suitable electromagnetic properties. BF33 exhibits a relative permittivity (ϵ_r) of 4.4 and a loss tangent $\tan\delta = 0.018$ at D-band frequencies. The PIGRA was designed and optimized on a glass-based PCB substrate with a relative permittivity of $\epsilon_r = 6.5$. The proposed concept is demonstrated through two implementations. The single-radiator design was implemented as a glass-on-glass (GoG) solution to demonstrate the feasibility of integrating the proposed PIGRA into an MMIC package, as illustrated in Figure 3. The PIGRA was fabricated using laser-induced deep etching (LIDE) technology, and the glass PCB substrate was metallized using physical vapor deposition (PVD) followed by an electroplating process.

The PIGRA is fed by a coplanar waveguide (CPW) and excited through a slot-coupling technique at the PIGRA–PCB interface on the base side (Figure 7). The dimensions of the CPW feed line and the coupling slot were optimized to minimize insertion loss while maximizing the antenna impedance matching performance. The second implementation is a 4 × 4 planar array fabricated on a two-layer Rogers CLTE substrate. The 16 PIGRA elements are excited in phase through a slot-coupled feeding technique, using a microstrip line structure (Figures 8 and 9). To facilitate integration with other front-end components, such as amplifiers, phase shifters, filters, transceivers, and RF test probes, which typically employ ground-signal-ground (GSG) pads with 100 or 150 µm pitch, a low-loss wideband CPW-to-microstrip transition was designed (Figure 8, label ①). The microstrip feed network distributes the input signal through 15 Wilkinson power dividers, providing a 1-to-16 equal-power split, with minimized loss. The resulting array achieves a peak realized gain of 15 dBi while maintaining a −10 dB impedance bandwidth across the D-band under a 50 Ω system impedance.

A probe-based antenna measurement (Figure 14) at Karlsruhe Institute of Technology (KIT) was used to evaluate the RF performance of both designs. The antenna measurement system is a far-field single-probe antenna measurement system, capable of measurements up to 325 GHz [25].

The main contributions of this work are summarized as follows:

- A novel glass-based pyramidal inverted DRA enabling ultra-wideband D-band operation.
- A GoG single-element demonstrator suitable for AiP integration.
- A low-loss 4 × 4 array incorporating an integrated CPW-to-microstrip transition and Wilkinson feed network.
- Experimental validation of both implementations, demonstrating more than 40% impedance bandwidth and a peak realized gain of 15 dBi.

The paper is organized as follows. The second section details the design of the PIGRA, starting with the single-element analysis and extending it to a 4 × 4 array configuration. The third section presents the manufacturing and assembly procedures. The fourth section reports the simulated and measured performance of both implementations, namely the single-element GoG and the array configuration. The fifth section concludes the paper.

Downloaded from https://www.cambridge.org/core. Karlsruher Institut fuer Technologie (KIT), on 19 Nov 2026 at 11:26:45, subject to the Cambridge Core terms of use, available at https://www.cambridge.org/core/terms. https://doi.org/10.1017/S1759078726103948

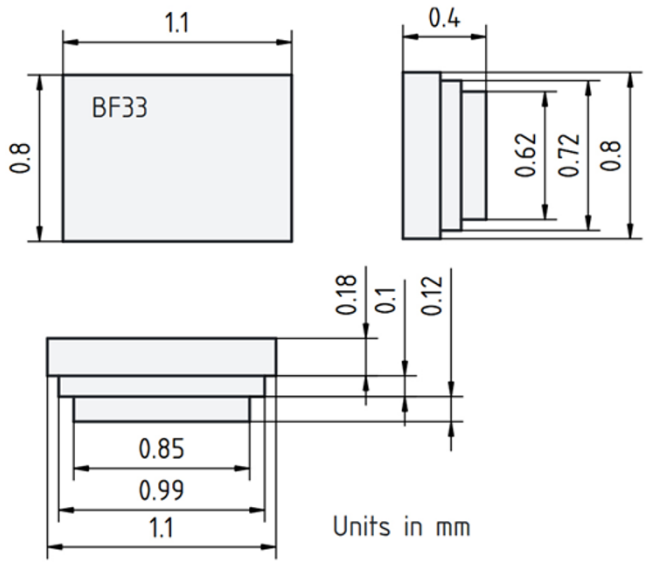


Figure 4. Proposed PIGRA geometry and dimensions.

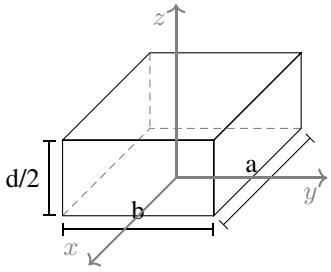


Figure 5. Illustration of the RDRA on a metal ground plane.

Design

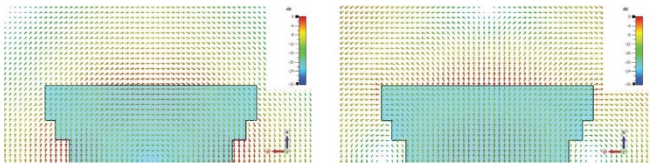
PIGRA on glass PCB

The PIGRA is a single-piece BF33 glass DRA consisting of three stacked rectangular cuboids that form an inverted pyramidal geometry (Figure 4). The smaller base is attached to the PCB, as illustrated in Figures 1 and 2(a).

To determine the dimensions of the PIGRA, the design begins with the analysis of an equivalent rectangular dielectric resonator antenna (RDRA). The resonator height is constrained by the available glass slab thickness of 0.5 mm, which is subsequently reduced to 0.4 mm through the LIDE process.

The RDRA is a well-studied structure [8] whose resonant characteristics can be estimated using the dielectric waveguide model (DWM) [27] or through the transverse resonance technique [29, 30], and subsequently verified through full-wave eigenmode analysis [28]. According to DWM, an RDRA is typically designed such that its first three or four resonant modes lie within the desired operating frequency band [26]. The inverted pyramidal geometry of the PIGRA is then derived from the equivalent RDRA to support the excitation of multiple resonant modes over the frequency range, thereby enhancing the impedance bandwidth without increasing the antenna footprint.

The DWM is applied to the geometry illustrated in (Figure 5). In this model, the resonator has dimensions a, b, and $d/2$, which represent the width, length, and height of the dielectric resonator



(a): E-Field of $TE^{y}_{1\delta1}$ mode. (b): H-Field $TM^{y}_{2\delta1}$ mode.

Figure 6. PIGRA electric- and magnetic-field distributions.

on a metal ground, respectively. The equivalent isolated dielectric resonator [26] has the dimensions a, b, and d. To determine the resonant modes, the analysis assumes perfect magnetic wall (PMW) boundary conditions on the vertical faces ($x = \pm a/2$, $y = \pm b/2$) of the resonator, while a perfect electric wall, representing the metal ground, and open boundary conditions are applied to the remaining faces ($z = 0$ and $z = d/2$, respectively). Under the PMW assumption, the boundary conditions for the vertical faces are given by

$$PMW : \begin{cases} \mathbf{E} \cdot \mathbf{u} = 0, \\ \mathbf{H} \times \mathbf{u} = 0, \end{cases} \tag{1}$$

where $\mathbf{E}$, $\mathbf{H}$, and $\mathbf{u}$ denote the electric field, magnetic field, and the normal vector to the corresponding faces, respectively. Consequently, the eigenvalues problem yields the transverse wavenumbers

$$k_x = m\pi/a, k_y = n\pi/b, \tag{2}$$

where m and n are the modal indices. By considering an equivalent transmission line (ETL) along z, the transverse admittance resonance condition ($Y_t = \overleftarrow{Y_t} + \overrightarrow{Y_t} = 0$), together with the dispersion equation ($\mathbf{k} \cdot \mathbf{k} = \omega^2\epsilon\mu$), results in the following transcendental equation [29, 30]:

$$k_z \tan(k_z d/2) = \sqrt{(\epsilon_r - 1)k_0^2 - k_z^2} \tag{3}$$

The solutions of (3) correspond to the resonance conditions of the ETL and, consequently, to the resonant frequencies associated with the mode $TE^{z}_{mn\delta}$ family. However, the electric field can be decomposed along three orthogonal directions (x, y, z), giving rise to transverse modes along each of the three dimensions (TE^{x}, TE^{y}, TE^{z}) [26]. The estimated resonance frequency of the fundamental ($TE^{z}_{11\delta}$) mode is approximately 129 GHz, using a relative permittivity $\epsilon_r = 4.5$ and dimensions $a = 1.25$ mm, $b = 0.8$ mm, and $d/2 = 0.5$ mm. Since the isolated resonator [26] satisfies $a > d > b$, rather than the $a > b > d$ condition considered by Marcatili [27], the classical modal ordering is not directly applicable. Therefore, the resonant modes are identified using the DWM and subsequently confirmed by full-wave eigenmode analysis in CST Microwave Studio.

According to Stevenson [31] and Van Bladel [32], not all resonant modes of an electrically small dielectric resonator contribute to radiation. For resonators characterized by high relative permittivity and a geometry of revolution, only specific resonant modes are capable of radiating efficiently, whereas other modes remain predominantly confined within the dielectric material. As the dielectric permittivity decreases, resonant modes become less well defined, and hybrid modes may appear [33]. Therefore, resonators made of low-permittivity materials are preferable for antenna applications.

Downloaded from https://www.cambridge.org/core. Karlsruher Institut fuer Technologie (KIT), on 19 Nov 2026 at 11:26:45, subject to the Cambridge Core terms of use, available at https://www.cambridge.org/core/terms. https://doi.org/10.1017/S1759078726103948

Since the PIGRA utilizes a low-permittivity glass with $\epsilon_r = 4.5$, and its geometry is not a solid of revolution, fully confined modes are not supported. Finite element method eigenmode analysis indicates that a conventional rectangular DRA of equivalent volume supports only three to four modes within the operating band, as illustrated in Table 1. The first RDRA mode is approximately 7 GHz higher than the analytical prediction. The first five resonant modes of the PIGRA, listed in Table 1, are distributed across the operating bandwidth and exhibit quasi-transverse field characteristics. This demonstrates that the PIGRA mode distribution across the operating band was optimized by tuning its cross-sectional profile. The electric field distribution of the first and second modes is shown in Figure 6, and the properties of the first five modes are summarized in Table 1. The fundamental $TE^y_{1\delta1}$ mode can be modeled as a set of in-phase y-directed magnetic dipoles on the lateral faces ($x = \pm a/2$), together with a y-directed electric dipole near the PIGRA base ($z = 0$). However, only the magnetic dipole associated to $TE^y_{1\delta1}$ mode contributes to radiation, while the electric dipole is suppressed due to cancellation by its ideal image in the conducting ground plane. The second mode ($TE^y_{2\delta1}$) can be represented by a magnetic current ribbon flowing around the lateral faces of the PIGRA. This distribution corresponds to a combination of a z-directed magnetic dipole and a z-directed electric dipole.

The slot-aperture coupling technique (Figure 7) is utilized to excite the PIGRA through a 50 Ω CPW line on a single-layer glass PCB. The slot geometry is optimized to match the input impedance of the PIGRA to the characteristic impedance of the CPW line. The slot length is approximately a half-wavelength in glass at 120 GHz. All geometric measured parameters are summarized in Figure 4, Figure 7, and Table 2. At the PCB edge, the CPW line is tapered to match the GSG probe pitch of 100 µm. The PCB thickness h was selected to be 0.1 mm to suppress the excitation of surface-wave modes [28] within the operating band. For a grounded dielectric substrate, the cutoff condition for the first surface mode is given by

$$h < \lambda_0/(4\sqrt{\epsilon_r - 1}), \quad for \quad TE_1 \tag{4}$$

where λ_0 is the free-space wavelength and $\epsilon_r = 6.5$ is the substrate relative permittivity, with a measured relative permittivity of $\epsilon_r = 6.5$ and a $\tan\delta$ of 0.02. With the fixed CPW height, the CPW width-to-gap ratio was optimized to match 50 Ω subject to the constraint that the minimum gap is set by the laser beam width of the manufacturing machine, which is around 20 µm at the focal point. The PCB metallized layer was modeled with a conductivity of $\sigma = 4 \times 10^7$ S/m, which corresponds to approximately 70 % of the conductivity of annealed copper.

Another parameter affecting the antenna impedance and, consequently, the gain is the adhesive layer thickness at the PIGRA–PCB interface, together with the CPW gap. The glue thickness was simulated in the range of 5–10 µm, and the best S-parameter performance is observed at around 7 µm. This is attributed to the adhesive shrinkage during assembly and curing, which requires process optimization by adjusting the initial glue thickness, the applied assembly force during the resonator placement, and the thermal shrinkage during curing. Such optimization is compatible with mass-production processes.

4 × 4 *planar array on Rogers CLTE PCB*

The array implementation is based on the previously designed single radiating element (PIGRA). The array design begins with the selection of the array topology. A planar square array is adopted because it provides high directivity and aperture efficiency while maintaining a compact and symmetric layout (Figures 8 and 9). The symmetric configuration facilitates the design of a low-loss, equal-path feed network for all 16 radiating elements, ensuring uniform amplitude and phase excitation. In addition, the regular element spacing provides stable radiation characteristics and low side-lobe levels across the operating frequency band. A 4 × 4 rectangular array configuration is selected with an element spacing of 1.30 mm, which corresponds to $0.61\lambda_0$ spacing at the center frequency band (140 GHz). Under uniform amplitude and phase excitation, this configuration theoretically provides an array gain (array gain factor) increase of 12 dB compared with a single

Table 1. Eigenmodes of R-DRA and PIGRA

Mode	RDRA	PIGRA	Type
1	136.0 GHz	126.2 GHz	$TE^y_{1\delta1}$
2	145.0 GHz	127.6 GHz	$TE^y_{2\delta1}$
3	170.4 GHz	133.3 GHz	$TM^y_{2\delta1}$
4	194.5 GHz	166.2 GHz	$TE^y_{1\delta2}$
5	–	167.2 GHz	$TM^y_{3\delta1}$
6	–	178.5 GHz	HEM^y

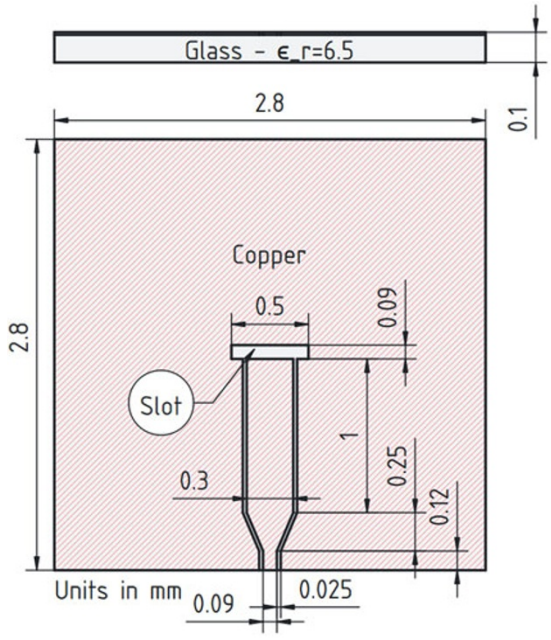


Figure 7. Single-radiator BF33 PCB dimensions.

Table 2. Measured dimensions in mm

Part	Length	Width	Height
PIGRA	1.10	0.80	0.41
PCB	2.80	2.80	0.10
	Length	Width	Gap
CPW	1.38	0.30	0.025
CPW@probe	0.125	0.08	0.025
Slot	0.50	0.09	-

Downloaded from https://www.cambridge.org/core. Karlsruher Institut fuer Technologie (KIT), on 19 Nov 2026 at 11:26:45, subject to the Cambridge Core terms of use, available at https://www.cambridge.org/core/terms. https://doi.org/10.1017/S1759078726103948

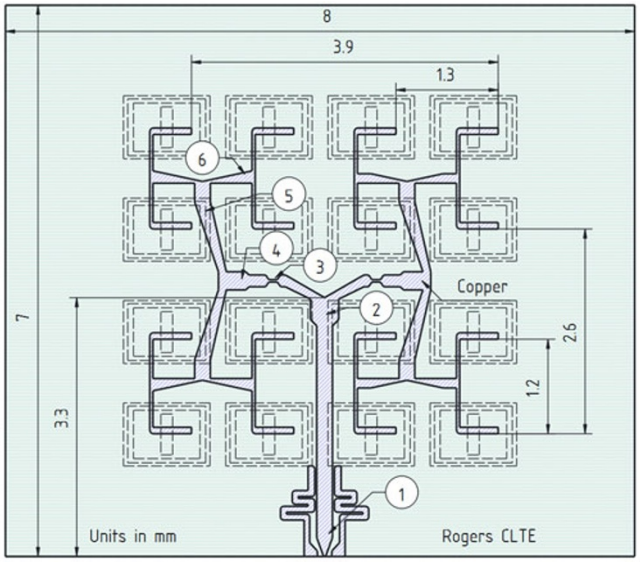


Figure 8. PCB bottom-layer feed network of the 4×4 array.

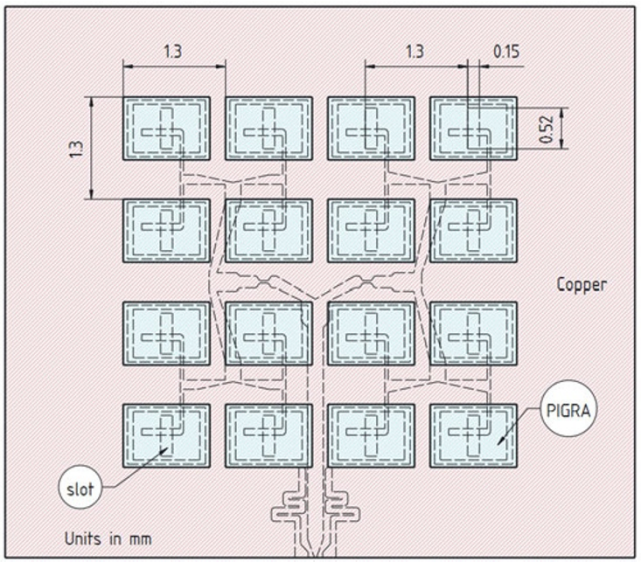


Figure 9. PIGRA element arrangement on the PCB top-layer of the 4×4 array.

PIGRA element. The element spacing was selected as a trade-off between aperture efficiency, mutual coupling, and the requirement of keeping the inter-element spacing below one free-space wavelength (λ_0) to suppress grating lobes. This corresponds to an inter-element spacing of $0.61\lambda_0$, which allows a potential scanning angle of approximately $\pm 40^\circ$, according to

$$\theta_{\max} = \arcsin\left(\frac{\lambda_0}{d} - 1\right). \tag{5}$$

The feed network was designed on a Rogers CLTE substrate with a thickness of 76.2 µm, a relative permittivity of 2.98, and a loss tangent ($\tan\delta$) of 0.0021. The CLTE substrate incorporates two copper layers, each with a thickness of 17.5 µm. The overall board dimensions are 7 mm by 8 mm. The radiating elements are coupled to the microstrip feed network through slot apertures (Figures 8 and 9). The objective of the feed network illustrated in Figure 8 is to distribute the RF signal from the GSG probe pads with a pitch of 100 µm to the 16 coupling slots, while minimizing the network loss over the operating bandwidth and maintaining equal electrical path lengths. The microstrip feed network begins with a novel broadband via-less CPW-to-microstrip transition (Figure 8, label ①), designed to match the GSG probe pitch. This transition was optimized using a back-to-back configuration over the operating band with a reference impedance of 50 Ω. The RF signal is equally divided into 16 lines using 15 broadband Wilkinson power dividers. The impedance matching within the feed network is achieved using quarter-wave ($\lambda/4$) impedance transformers (labels ② and ④), multi-section matching transformers (label ③), and tapered transmission-line sections (labels ④ and ⑥) to minimize feed-network loss. No higher-order modes or mode conversion associated with the CPW-to-microstrip transition were observed, due to the tight coupling between the ground pads and the signal line. The ground-to-signal gap is 18 µm. The coupling slots are 20 µm wider than the single-element design (0.52 vs 0.5 mm).

Manufacturing and assembly

The BF33 PIGRA is manufactured using the LID process developed by LPKF. The BF33 glass sheet has an initial thickness of 0.5 mm and is reduced to 0.4 mm after the chemical etching, laser ablation, and polishing process. PIGRA measured height was 0.41 mm, with a top surface measuring 1.10 mm × 0.80 mm. The glass dielectric resonator manufacturing process is shown in Figure 10(a). The steps are: material preparation, laser ablation and wet etching, and final cleaning.

The single radiator GoG (Figure 11) implementation employs a glass substrate with a permittivity of 6.5 ($tan\delta = 0.003$), a roughness of approximately 1 nm, and a thickness of 0.1 mm. The glass substrate is coated through a two-step metallization process. The first step utilizes PVD of copper on a nickel adhesion layer of approximately 10 nm, with a final total thickness of approximately 100 nm. Since the skin depth at D-band frequency is approximately of 190 nm, a second metallization step is required to increase the conductor thickness and consequently to reduce conductor loss. Electroplating is subsequently performed, where an electric current reduces the dissolved copper ions to build a uniform metal coating on the previously sputtered glass substrate, which acts as the electrode in the copper bath. The metallized glass substrate is structured with a CPW transmission line ending with the PIGRA feeding slot, and laser-cut with a conventional laser machine. The laser machine has a laser spot diameter of 20 µm at the focal point. The glass substrate manufacturing process at KIT is shown in Figure 10(b). The PCB and PIGRA are assembled at KIT using a die attach foil, AFN303, from Furukawa, with a pre-cured thickness of 10 µm and a permittivity in the range of 2.0–2.2. The Finetech Fineplacer Pico is utilized for this operation. The assembled sample is cured for one hour at 120°C (Figure 10(c)).

The 4×4 PIGRA array (Figure 12) on a Rogers CLTE PCB follows a similar manufacturing and assembly process. Unlike the GoG implementation, the Rogers CLTE PCB is supplied with two pre-metallized copper layers, eliminating the need for the PVD and electroplating processes. Small alignment errors were observed during the assembly of the PIGRA onto the PCB.

Simulation and measurements results

The GoG PIGRA concept and the 4×4 array were simulated using CST Microwave Studio. The finite-difference time-domain

Downloaded from https://www.cambridge.org/core. Karlsruher Institut fuer Technologie (KIT), on 19 Nov 2026 at 11:26:45, subject to the Cambridge Core terms of use, available at https://www.cambridge.org/core/terms. https://doi.org/10.1017/S1759078726103948

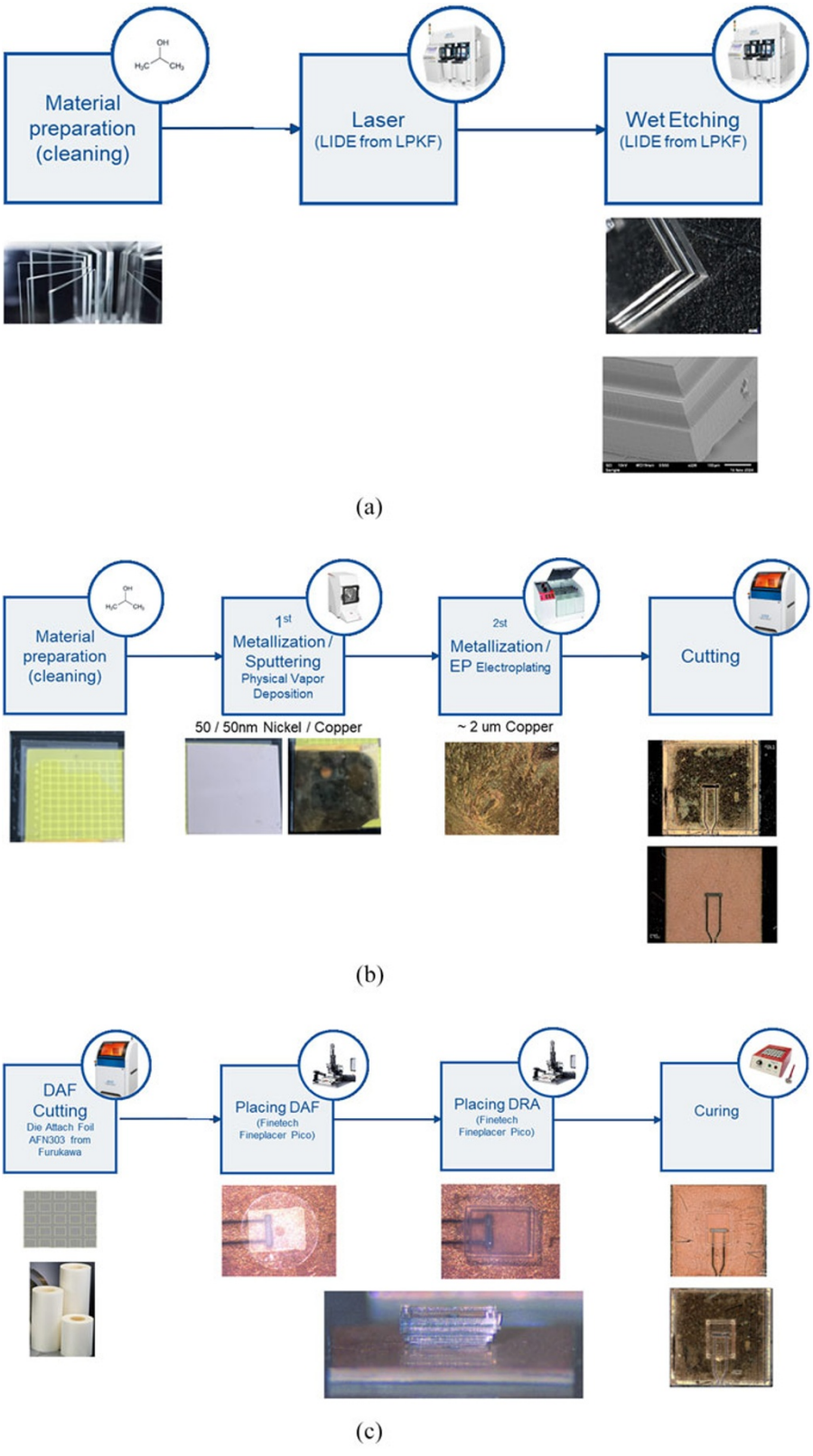


Figure 10. PIGRA manufacturing process (a), glass PCB fabrication (b), and assembly process (c).

solver with a hexahedral mesh was used. The simulation models consisted of approximately 1.2 and 68 million mesh cells for the single radiator and array, respectively. The radiation characteristics were measured at the KIT mmWave laboratory using a spherical single-probe-based antenna measurement system (Figure 14) [25]. The system is based on a Keysight PNA-X N5242B vector network analyzer with a N5261A mmWave controller, a VDI WR6.5-VNAX D-band frequency extender, and a GGB Industries 170-GSG-100-BT-M probe. Measurements were performed under far-field conditions. For the antenna under test (AUT) dimensions

Downloaded from https://www.cambridge.org/core. Karlsruher Institut fuer Technologie (KIT), on 19 Nov 2026 at 11:26:45, subject to the Cambridge Core terms of use, available at https://www.cambridge.org/core/terms. https://doi.org/10.1017/S1759078726103948

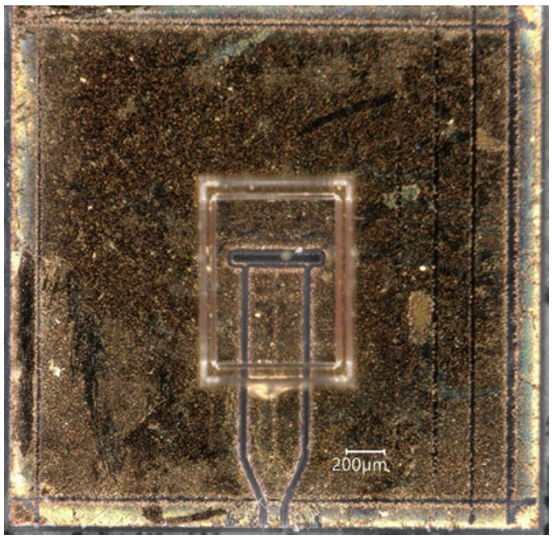
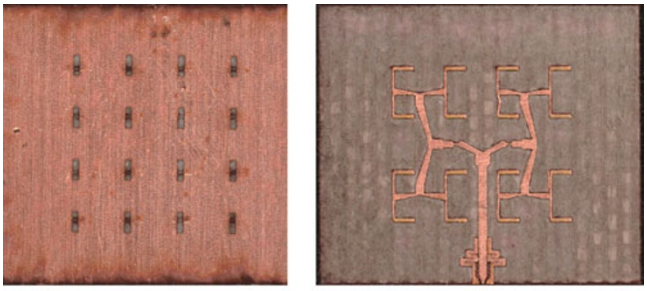
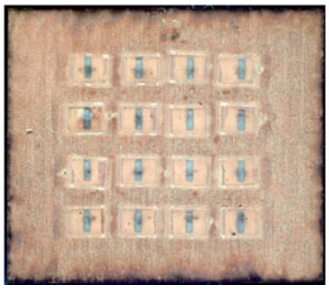


Figure 11. PIGRA assembled on a PVD-metallized and patterned 100 µm glass substrate.



(a): Top layer of the PCB. (b): Bottom layer of the PCB.



(c): Assembled sample.

Figure 12. Fabricated 4×4 array sample on a Rogers CLTE 76 µm PCB.

of 7 mm × 8 mm (maximum dimension $D = 8$ mm, neglecting the GSG probe influence), the Fraunhofer distance at 140 GHz ($\lambda_0 = 2.14$ mm) is

$$R_{\mathrm{FF}} \geq \frac{2D^2}{\lambda_0}, \tag{6}$$

$$R_{\mathrm{FF}} \geq \frac{2(8\,\mathrm{mm})^2}{2.14\,\mathrm{mm}} \approx 59.8\,\mathrm{mm} \approx 60\,\mathrm{mm}. \tag{7}$$

Since the distance between the probe antenna and the AUT is 700 mm, the far-field criterion was satisfied. Gain calibration was

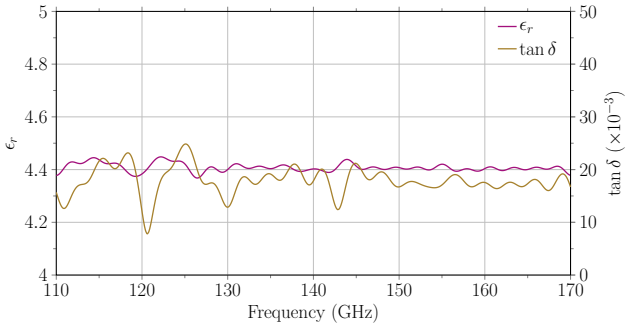


Figure 13. Measured dielectric properties of a 0.5 mm BF33 glass sample.

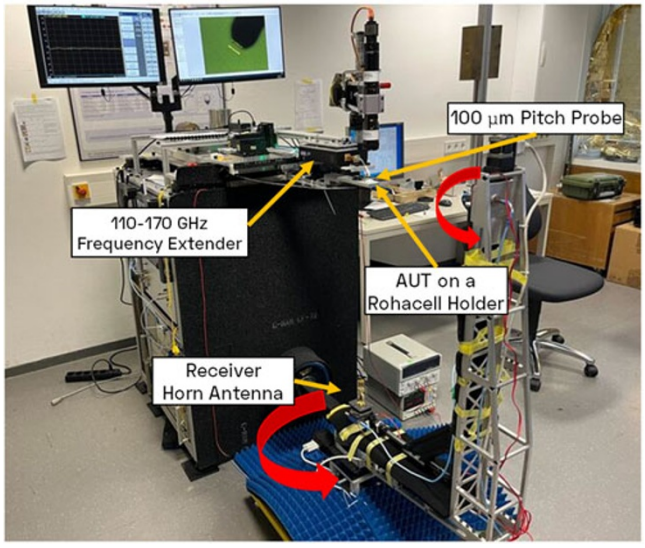


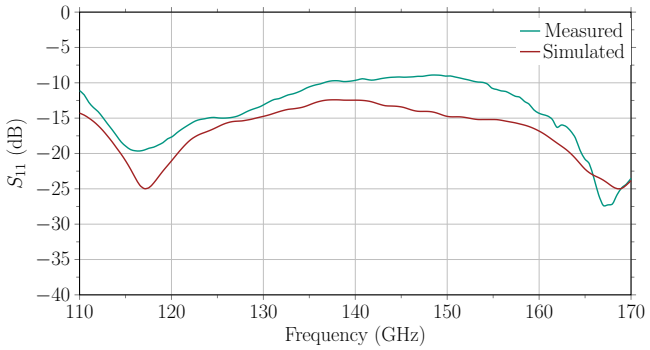
Figure 14. mmWave antenna measurement setup at KIT.

performed using the gain substitution method [35] with two standard WR6 horn antennas from Mi-Wave. A one-port on-wafer SOL calibration was carried out using a GGB Industries CS-15 calibration substrate. The AUT was supported by a low-permittivity polymethacrylimide (ROHACELL 51) foam sheet to minimize its influence on the radiation performance.

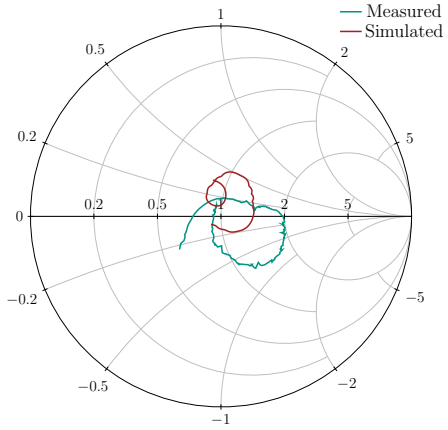
During the design phase, it was necessary to characterize the BF33 material for an accurate design. The material's dielectric characterization was performed using the Swissto12 Material Characterization Kit, which uses a circular waveguide technique. The material samples were placed between the circular tapered waveguide sections. The measured BF33 relative permittivity and loss tangent (*tanδ*) are approximately 4.4 and 0.02, respectively (Figure 13).

The measured and simulated S-parameters and Smith chart are shown in Figure 15. The −10 dB impedance bandwidth clearly covers the whole D-band, with minor deterioration at the center of the frequency band. The two return-loss minima are around 118 and 167 GHz. The simulated and measured S_{11} show good agreement, with a slightly worse impedance matching level around 150 GHz. The measured Smith chart (Figure 15(b)) shows two under-coupled resonances around 167 and at 135 GHz, which are linked to the first and the third resonant mode. The resonance coupling depends on the relative PIGRA positioning over the feeding slot and the feeding slot size due to the mechanical tolerances. The

Downloaded from https://www.cambridge.org/core. Karlsruher Institut fuer Technologie (KIT), on 19 Nov 2026 at 11:26:45, subject to the Cambridge Core terms of use, available at https://www.cambridge.org/core/terms. https://doi.org/10.1017/S1759078726103948



(a) Measured and simulated $|S_{11}|$.



(b) Measured and simulated S_{11} on the Smith chart.

Figure 15. Comparison between measured and simulated reflection coefficient of the single PIGRA radiator.

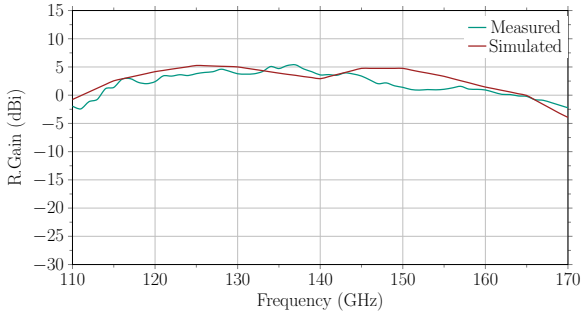


Figure 16. Measured and simulated realized gain of the single PIGRA.

measured and simulated vertically polarized far-field radiation patterns at 138 GHz are shown in Figure 17. The main beam is directed towards broadside (zenith $+z$) with a half-power beamwidth of approximately 60°. Minor ripples in the main lobe are primarily attributed to scattering from the PCB edges. The simulated efficiency exceeds −0.8 dB (83 %) throughout the operating band. In Figure 16, the PIGRA realized gain in the zenith direction (+Z axis) is shown. The peak gain is approximately 5.8 dBi at 135 GHz, including GSG-to-CPWG and CPWG line losses. The gain decreases toward the D-band edges due to the frequency-dependent shift of the radiation-pattern peak. The measured and simulated performance of the 4 × 4 PIGRA array is presented in

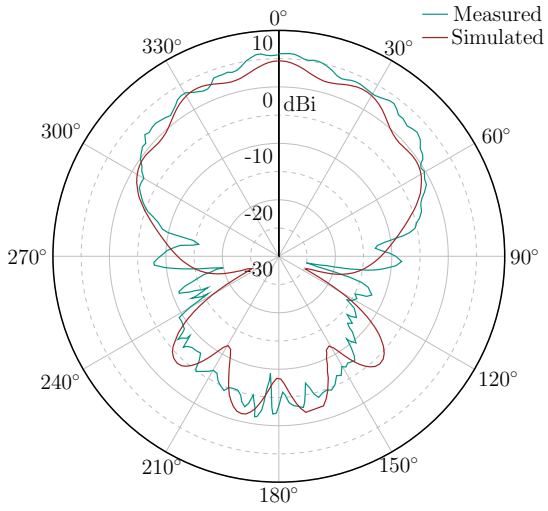


Figure 17. PIGRA radiation pattern at 138 GHz, transversal cut, V-pol.

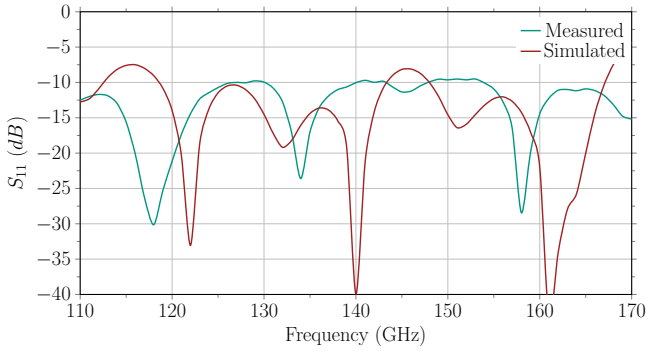


Figure 18. $|S_{11}|$ of the 4 × 4 PIGRA array.

Figures 18 and 19. The S_{11} curves shown in Figure 18 are below −10 dB across almost the whole D-band frequency range. The measured broadside realized gain of the vertically polarized (V-pol.) component reaches a peak of 15 dBi in Figure 19 at 128 GHz. The cross-polarized (H-pol.) component remains 20–40 dB below the co-polarized (V-pol.) component across the operating band. The measured radiation patterns at peak-gain frequency are in good agreement with the simulation (Figure 20). The main beam is directed towards broadside, with a measured front-to-back ratio of approximately 7–8 dB. The small deviations between simulation and measurement are mainly attributed to the influence of the GSG probe. A slight asymmetry is observed in the transverse-plane radiation patterns (Figure 20(a) and (c)), primarily caused by the feed network and the probe influence. The influence of the assembly tolerances was also investigated. The measured positioning error of the glass radiator was below 130 µm, with angular misalignment below 4° (Figure 21).

Conclusion

A new wideband glass-based antenna concept for D-band applications has been presented. To the best of the authors' knowledge, this work demonstrates for the first time a wideband glass-based GoG antenna concept in the D-band, covering a wide frequency

Downloaded from https://www.cambridge.org/core. Karlsruher Institut fuer Technologie (KIT), on 19 Nov 2026 at 11:26:45, subject to the Cambridge Core terms of use, available at https://www.cambridge.org/core/terms. https://doi.org/10.1017/S1759078726103948

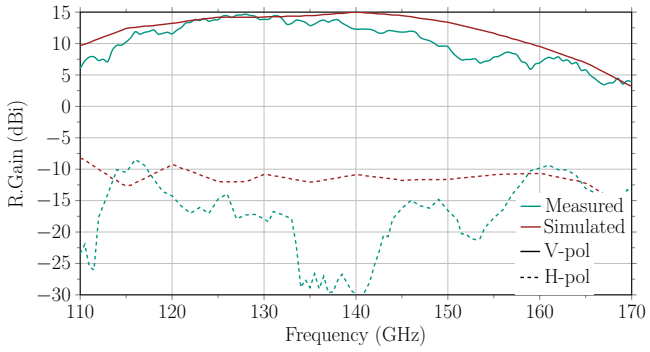
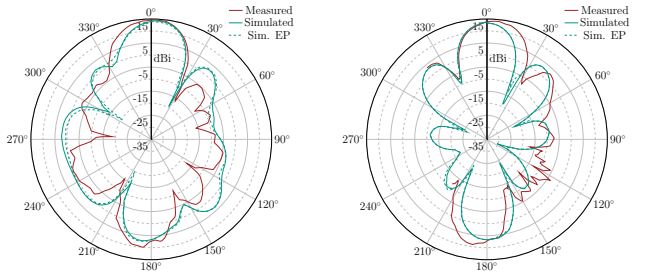
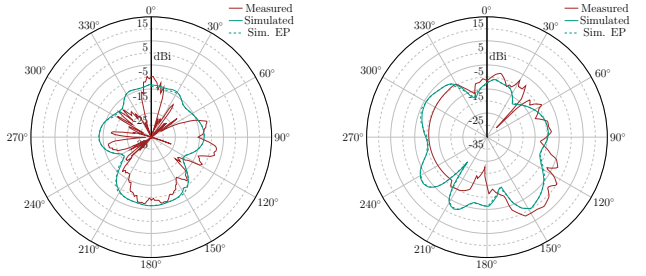


Figure 19. Realized gain of the 4 × 4 PIGRA array.

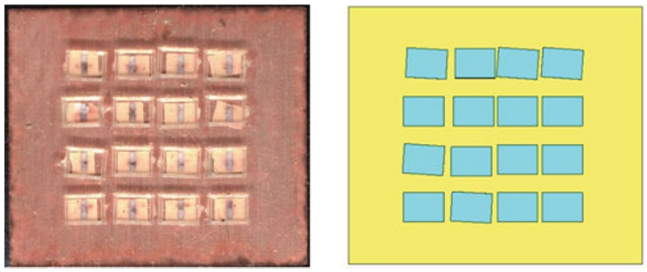


(a): Transversal plane, V-pol. (b): Longitudinal plane, V-pol.



(c): Transversal plane, H-pol. (d): Longitudinal plane, H-pol.

Figure 20. 4 × 4 PIGRA array radiation pattern at 128 GHz.



(a): 4 × 4 array prototype (b): 4 × 4 array CST model

Figure 21. Radiator positioning error.

range from 110 to 170 GHz, with a peak realized gain of 5.8 dBi for the single radiator and 15 dBi for the 4 × 4 array implemented on a 76 μm-thick CLTE substrate.

The proposed approach is compared with recently reported dielectric resonators operating in D-band (Table 3). This work, compared to the work done by [34, 36, 37], shows that the proposed

Table 3. State-of-the-art of D-band DRAs as single element and in array configuration

Number of DRAs	DRA shape	Material/permittivity	Freq. (GHz)	Relative bandwidth %	Realized peak gain (dBi)	reference
Single	Rectangular	Alumina / 10	123–137	11	2.7	[34]
2 Stacked	Rectangular	Alumina / 10	123–137	11	4.7	[34]
Single	Rectangular	Alumina / 9.8	115–162	34	5	[36]
Single	Pyramidal	Glass BF33 / 4.4	110–170	43	5.8	**This work**
array 4 × 4	Rectangular	Glass BF33 / 4.4	135–146	8	13.2	[37]
array 4 × 4	Pyramidal	Glass BF33 / 4.4	118–168	35	15	**This work**

Downloaded from https://www.cambridge.org/core. Karlsruher Institut fuer Technologie (KIT), on 19 Nov 2026 at 11:26:45, subject to the Cambridge Core terms of use, available at https://www.cambridge.org/core/terms. https://doi.org/10.1017/S1759078726103948

pyramidal inverted glass resonator antenna achieves the widest bandwidth and the highest peak gain, both as a single radiator and in an array configuration. This is due to the multimode excitation in the operating D-band.

The glass resonator radiator was fabricated using LIDE technology, while the glass-based PCB was metallized using a two-step process consisting of PVD and electroplating. These fabrication processes are based on mature semiconductor-compatible technologies.

This work demonstrates, for the first time, a wideband glass-based D-band antenna integrated on a glass substrate metallized through PVD and electroplating processes. In particular, it validates the feasibility of 2.5D glass micromachining beyond 100 GHz. The presented results represent a significant advancement toward GoG AiP solutions for sub-THz applications, enabling potential applications in 6G communication systems, beyond-6G technologies, and radar sensing.

Funding statement. This work is supported financially by the Federal Ministry of Education and Research of Germany, through the projects ESSENCE (grant number 16KISK173) and X-TREME 6G (grant number 101192681).

Competing interests. None declared.

References

1. **Faliero M, Quint A, Valenziano L, Bekker E, Zwick T and Bhutani A** (2025) A wideband glass resonator antenna as AiP concept for sub-THz application. In *55th European Microwave Conference (EuMC)*. https://doi.org/10.23919/EuMC65286.2025.11235059
2. **Jung D, Park C-J, Kwon TS, Seo JW, Ahn B, Wi S-H and Na L** (2024) Terahertz antenna-in-package design and measurement for 6G communications systems. *IEEE Transactions on Antennas and Propagation* **72**(2), 1085–1096. https://doi.org/10.1109/TAP.2023.3320276
3. **Lee SY, Lee D, Zhang Y, Hong W and Ghalichechian N** (2025) History and the latest progress in antenna packaging technology: Part 1: Multilayer solutions. *IEEE Antennas and Propagation Magazine* **67**(3), 48–61. https://doi.org/10.1109/MAP.2025.3560852
4. **Maiwald T, Li T, Hotopan G-R, Kolb K, Disch K, Potschka J, Haag A, Dietz M, Debaillie B, Zwick T, Aufinger K, Ferling D, Weigel R and Visweswaran A** (2023) A review of integrated systems and components for 6G wireless communication in the D-band. *Proceedings of the IEEE* **111**(3), 220–256. https://doi.org/10.1109/JPROC.2023.3240127
5. **Hyltin TM** (1965) Microstrip transmission on semiconductor dielectrics. *IEEE Transactions on Microwave Theory and Techniques* **13**(6), 777–781. https://doi.org/10.1109/TMTT.1965.1126104
6. **Watanabe AO, Ali M, Sayeed SYB, Tummala RR and Pulugurtha MR** (2021) A review of 5G front-end systems package integration. *IEEE Transactions on Components, Packaging and Manufacturing Technology* **11**(1), 118–133. https://doi.org/10.1109/TCPMT.2020.3041412
7. **Zhang YP and Liu D** (2009) Antenna-on-chip and antenna-in-package solutions to highly integrated millimeter-wave devices for wireless communications. *IEEE Transactions on Antennas and Propagation* **57**(10), 2830–2841. https://doi.org/10.1109/TAP.2009.2029295
8. **Petosa A and Ittipiboon A** (2010) Dielectric resonator antennas: A historical review and the current state of the art. *IEEE Antennas and Propagation Magazine* **52**(5), 91–116. https://doi.org/10.1109/MAP.2010.568751010
9. **Koch M, Schönecker A, Kohl C, Breun S, Weigel R and Franchi N** (2025) sub-THz circuit and system architectures for communication and sensing in 6G and beyond. In *2025 Asia-Pacific Microwave Conference (APMC)*. Jeju, Korea, Republic of, pp. 1–3. https://doi.org/10.1109/APMC65046.2025
10. **Richtmyer RD** (1939) Dielectric resonators. *Journal of Applied Physics* **10**(6), 391–398. https://doi.org/10.1063/1.1707320
11. **Nomura S** (1983) Ceramics for microwave dielectric resonator. *Ferroelectrics* **49**(1), 61–70. https://doi.org/10.1080/00150198308244666
12. **Cohn SB** (1968) Microwave bandpass filters containing high-Q dielectric resonators. *IEEE Transactions on Microwave Theory and Techniques* **16**(4), 218–227. https://doi.org/10.1109/TMTT.1968.1126654
13. **Van Bladel J** (1975) On the resonances of a dielectric resonator of very high permittivity. *IEEE Transactions on Microwave Theory and Techniques* (**23**)2, 199–208. https://doi.org/10.1109/TMTT.1975.1128528
14. **Long S, McAllister M and Shen L** (1983) The resonant cylindrical dielectric cavity antenna. *IEEE Transactions on Antennas and Propagation* **31**(3), 406–412. https://doi.org/10.1109/TAP.1983.1143080
15. **Guillon P** (1985) The dielectric resonators and their applications in microwave circuits. In *1985 15th European Microwave Conference*. Paris, France, pp. 77–86. https://doi.org/10.1109/EUMA.1985.333463
16. **Petosa A, Ittipiboon A, Antar YMM, Roscoe D and Cuhaci M** (1998) Recent advances in dielectric-resonator antenna technology. *IEEE Antennas and Propagation Magazine* **40**(3), 35–48. https://doi.org/10.1109/74.706069
17. **Smith H and Mayes P** (1987) Stacking resonators to increase the bandwidth of low-profile antennas. *IEEE Transactions on Antennas and Propagation* **35**(12), 1473–1476. https://doi.org/10.1109/TAP.1987.1144046
18. **Kishk AA, Ahn B and Kajfez D** (1989) Broadband stacked dielectric resonator antennas. *Electronics Letters* **25**(18), 1232–1233. https://doi.org/10.1049/el:19890826
19. **Luk KM, Leung KW and Chow KY** (1997) Bandwidth and gain enhancement of a dielectric resonator antenna with the use of a stacking element. *Microwave and Optical Technology Letters* **14**(4), 215–217. https://doi.org/10.1002/(SICI)1098-2760(199703)14:43.0.CO;2-M
20. **Lapierre M, Antar YMM, Ittipiboon A and Petosa A** (2005) Ultra wideband monopole/dielectric resonator antenna. *IEEE Microwave and Wireless Components Letters* **15**(1), 7–9. https://doi.org/10.1109/LMWC.2004.840952
21. **Simons RN and Lee RQ** (1993) Effect of parasitic dielectric resonators on CPW/aperture-coupled dielectric resonator antennas. In *IEE Proceedings H (Microwaves, Antennas and Propagation)*. https://doi.org/10.1049/ip-h-2.1993.0052
22. **Kakhki MB, Mousavirazi Z and Denidni TA** (2019) High gain ridge gap dielectric resonator antenna using FSS superstrates. In *2019 IEEE International Symposium on Antennas and Propagation and USNC-URSI Radio Science Meeting*. Atlanta, GA, USA, pp. 71–72
23. **Nasimuddin and Esselle KP** (2007) A low-profile compact microwave antenna with high gain and wide bandwidth. *IEEE Transactions on Antennas and Propagation* **55**(6), 1880–1883. https://doi.org/10.1109/TAP.2007.898644
24. **Keyrouz S and Caratelli D** (2016) Dielectric resonator antennas: Basic concepts, design guidelines, and recent developments at millimeter-wave frequencies. *International Journal of Antennas and Propagation*. https://doi.org/10.1155/2016/6075680
25. **Beer S and Zwick T** (2010) Probe based radiation pattern measurements for highly integrated millimeter-wave antennas. In *Proceedings of the Fourth European Conference on Antennas and Propagation*. Barcelona, Spain, pp. 1–5.
26. **Mongia K and Ittipiboon A** (1997) Theoretical and experimental investigations on rectangular dielectric resonator antennas. *IEEE Transactions on Antennas and Propagation* **45**(9), 1348–1356. https://doi.org/10.1109/8.623123
27. **Marcatili EAJ** (1969) Dielectric rectangular waveguide and directional coupler for integrated optics. *The Bell System Technical Journal* **48**(7), 2071–2102. https://doi.org/10.1002/j.1538-7305.1969.tb01166.x
28. **Pozar DM** (2021) *Microwave Engineering*, 5th Edn. Wiley.
29. **Felsen L and Marcuvitz N** (1973) *Radiation and Scattering of Waves*, Prentice-Hall, pp. 215–217.
30. **Sorrentino R and Mongiardo M** (2005) *Transverse Resonance Techniques*. *In* Encyclopedia of RF and Microwave Engineering. K. Chang (Ed.), John Wiley & Sons. https://doi.org/10.1002/0471654507.eme465
31. **Stevenson AF** (1953) Solution of electromagnetic scattering problems as power series in the ratio (dimension of scatterer)/wavelength

Downloaded from https://www.cambridge.org/core. Karlsruher Institut fuer Technologie (KIT), on 19 Nov 2026 at 11:26:45, subject to the Cambridge Core terms of use, available at https://www.cambridge.org/core/terms. https://doi.org/10.1017/S1759078726103948

Journal of Applied Physics **24**(9), 1134–1142. https://doi.org/10.1063/1.1721461

32. **Van Bladel J** (1975) The excitation of dielectric resonators of very high permittivity. *IEEE Transactions on Microwave Theory and Techniques* **23**(2) 208–217. https://doi.org/10.1109/TMTT.1975.1128529
33. **Chen C and Zaki KA** (1988) Hybrid mode dielectric resonators in microstrip. *18th European Microwave Conference*.
34. **Hou D, Xiong Y-Z, Goh W-L, Hu S, Hong W and Madihian M** (2012) 130-GHz on-chip meander slot antennas with stacked dielectric resonators in standard CMOS technology. *IEEE Transactions on Antennas and Propagation* **60**(9), 4102–4109. https://doi.org/10.1109/TAP.2012.2207077
35. **Kanda M** (1983) Techniques for accurate measurement of antenna gain. National Bureau of Standards (NBS), NBS Technical Note 598.
36. **Li T, Disch K, Haag A, Visweswaran A, Bhutani A and Zwick T** (2021) Design of wideband dielectric resonator antenna for D-band applications. In *International Symposium on Antennas and Propagation (ISAP)*.
37. **Bekker E, Yin J, Valenziano L, Lootze M, Schulz-Ruhtenberg M, Zwick T and Bhutani A** (2025) Precision manufacturing of glass dielectric resonator antennas for sub-THz applications using laser induced deep etching technology. *Electronics Letters* **61**(1), e70141. https://doi.org/10.1049/ell2.70141



Mario Faliero received the M.Sc. degree in telecommunication engineering from the University of Siena, Siena, Italy. Following a career in industry where he held several engineering and management roles within the European telecommunication and automotive sectors, he joined the Karlsruhe Institute of Technology (KIT), Karlsruhe, Germany, where he is currently a research assistant. His research activities focus on analytical and applied electromagnetics, antenna theory, and antenna design, with specific interests in artificial electromagnetic structures, wideband impedance layered structures, and soft and hard boundary materials.



Thomas Zwick (Fellow, IEEE) received the Dipl.-Ing. (M.S.E.E.) and the Dr.-Ing. (Ph.D.E.E.) degrees from the University Karlsruhe (TH), Germany, in 1994 and 1999, respectively. From 1994 to 2001, he was a research assistant at the Institut für Hochfrequenztechnik und Elektronik (IHE) at the University Karlsruhe (TH), Germany. In February 2001, he joined IBM as a research staff member at the IBM T. J. Watson Research Center, Yorktown Heights, NY, USA. From October 2004 to September 2007, Thomas Zwick was with Siemens AG, Lindau, Germany. During this period, he managed the RF development team for automotive radars. In October 2007, he became a full professor at the Karlsruhe Institute of Technology (KIT), Germany. He is the director of the Institut für Hochfrequenztechnik und Elektronik (IHE) at the KIT.



Akanksha Bhutani received the M.Sc. and Ph.D. degrees in electrical engineering and information technology from the Karlsruhe Institute of Technology (KIT), Karlsruhe, Germany, in 2012 and 2019, respectively. Since 2019, she has been leading the Antennas and Packaging research group at the Institute of Radio Frequency Engineering and Electronics, KIT. Her research work focuses on THz antennas and packaging for radar and wireless communication systems.

Downloaded from https://www.cambridge.org/core. Karlsruher Institut fuer Technologie (KIT), on 19 Nov 2026 at 11:26:45, subject to the Cambridge Core terms of use, available at https://www.cambridge.org/core/terms. https://doi.org/10.1017/S1759078726103948